The Astrophysical Journal, 869:31 (11pp), 2018 December 10 https://doi.org/10.3847/1538-4357/aae92d

EoS Dependence of the Relic Supernova Neutrino Spectrum

J. Hidaka[1,2], T. Kajino[2,3,4], and G. J. Mathews[2,5]
[1] Mechanical Engineering Department, Meisei University, 2-1-1 Hodokubo, Hino, Tokyo 191-8506, Japan
[2] National Astronomical Observatory of Japan 2-21-1 Osawa, Mitaka, Tokyo, 181-8588, Japan; jun.hidaka@meisei-u.ac.jp
[3] International Research Center for Big-Bang Cosmology and Element Genesis, and School of Physics and Nuclear Energy Engineering, Beihang University, Beijing 100191, People's Republic of China
[4] Department of Astronomy, School of Science, the University of Tokyo, 7-3-1 Hongo, Bunkyo-ku, Tokyo, 113-0033, Japan; kajino@nao.ac.jp
[5] Center for Astrophysics, Department of Physics, University of Notre Dame, Notre Dame, IN 46556, USA Japan; gmathews@nd.edu
Received 2018 February 7; revised 2018 September 12; accepted 2018 October 15; published 2018 December 7

Abstract

Understanding the mechanism of core-collapse supernova explosions requires knowledge of the nuclear equation of state (EoS). Recent multi-dimensional numerical simulations indicate that explosions are possible. Nevertheless, it is not yet fully understood which equation of state is realized in the proto-neutron star formed during SN explosions. We examine the EoS sensitivity of the relic supernova neutrino spectrum as a probe of the nuclear EoS. This sensitivity arises largely from the contribution to neutrino emission from failed supernovae. We consider a variety of astrophysical scenarios, which include different progenitor masses for a successful explosion, the cosmological star formation rate, starbursts, quiescent star formation, and the metallicity dependence of the initial mass function. We find that the EoS signature remains robust under a variety of conditions. We demonstrate the viability of future neutrino detectors to distinguish the nuclear EoS via the relic supernova neutrino spectrum.

Key words: diffuse radiation – neutrinos – stars: formation – stars: massive – supergiants – supernovae: general

1. Introduction

Recent progress in numerical supernova simulations has provided insight into the mechanism of core-collapse SN explosions. In particular, it is now known that there is a non-monotonic dependence of the explosion on progenitor mass (Pejcha & Thompson 2015; Sukhbold et al. 2016). Indeed, numerical investigations have revealed that the density profile of the progenitor core is an essential property to classify the outcome of the explosion. The so-called compactness parameter has been proposed as a key to understanding this physics (O'Connor & Ott 2011).

Moreover, there is observational evidence (Smartt 2009, 2015) suggesting that the mass of the red supergiant progenitor for core-collapse supernovae must be less than 16.5–18$M_{\odot}$. This Red Supergiant Problem could be related to the criteria for a successful SN in terms of the compactness parameter (Horiuchi et al. 2014).

We have studied (Mathews et al. 2014; Hidaka et al. 2016) the contribution to the relic supernova neutrino spectrum from different types of SNe. These previous works have shown that there is a clear EoS dependence in the spectrum. It is, however, crucial to clarify how sensitive these findings are to various astrophysical scenarios in order to quantify the EoS dependence of the RSN spectrum. For example, any change in the occurrence of core-collaped supernovae (CCSNe) versus failed supernovae (fSNe) obviously affects the expected neutrino spectrum. Thus, it is important to apply different criteria for a successful SN explosion and to analyze their effects on the RSN spectrum.

Moreover, the observational estimation of the cosmic star formation rate (SFR) is an involved procedure based upon different sources, e.g., UV light from galaxies and the far infrared (FIR) luminosity (Madau & Dickinson 2014). It also depends on modeling for the interpretation of the observational data, e.g., the fit to the spectral energy distribution (SED; Conroy 2013). Therefore, it is valuable to consider different SFR estimates and study their effects on the RSN spectrum.

The SFR also depends upon the choice of the stellar initial mass function (IMF). The IMF is a fundamental quantity not only for SFR estimation but also for the occurrence of each type of SN. A universal IMF, typically Salpeter-like IMF, is commonly assumed in almost every aspect of the astronomical derivation. Theoretical studies have attempted to derive this universality (Padoan et al. 1997; Padoan & Nordlund 2002). Nevertheless, a convincing theory for the universal IMF has not yet been established. Another uncertainty surrounding the IMF is its metallicity dependence. In general, cooler molecular clouds should more easily collapse to form stars. Therefore, metal-poor molecular clouds, which may be common at high redshift, could tend to form more massive stellar objects. This leads to the concept of a top-heavy IMF in the early universe, i.e., a z-dependent IMF.

In this article we investigate the EoS dependence of the RSN spectrum by applying a variety of scenarios as described above. We show that the EoS dependence is sufficiently robust that the relic supernova neutrino spectrum can be used to gain insight into the nuclear EoS for core-collapse supernova explosions almost independently of the many uncertainties in the astrophysical scenarios.

2. Progenitors and Occurrence of SNe

It is especially important to know which progenitors become which type of SN because each SN emits a different spectrum of neutrinos (see Mathews et al. 2014). Since the occurrence of SN1987A, there have been many investigations into neutrino emission based upon this SN. Many numerical simulations have been performed that produce supernova explosions similar to SN1987A. Recent progress in multi-dimensional supernova simulations has led to successful explosions (Lentz et al. 2015; Melson et al. 2015a, 2015b; Müller 2015) although they are not yet fully satisfactory. Nevertheless, there seems to

be a common feature in the relationship between the structure of the progenitor and successful explosions (Ugliano et al. 2012; Horiuchi et al. 2014; Nakamura et al. 2015; Pejcha & Thompson 2015; Ertl et al. 2016; Sukhbold et al. 2016). The density profile of progenitors is parameterized by a compactness parameter, and progenitors with greater compactness are less able to explode because they experience more accretion of material before the shock passes through the core.

In addition to this global trend of successful explosions, there is another phenomenon that successful/failed SNe occur with a non-monotonic dependence on progenitor mass (Ugliano et al. 2012; Pejcha & Thompson 2015; Ertl et al. 2016; Sukhbold et al. 2016). Previously, most studies of relic supernova neutrinos assumed definitive mass ranges within which a certain type of SN can occur (e.g., Horiuchi et al. 2009; Keehn & Lunardini 2012; Hidaka et al. 2016). Thus, SN occurrence was simply based upon adopted lower and upper mass limits of their progenitors. Based upon this new finding, however, one needs to re-evaluate the RSN spectrum by taking into account the sporadic dependence of the SN explosion on the progenitor mass.

In this study we follow the work of Pejcha & Thompson (2015) and adopt the fraction of failed SN, $f_{\rm fSN} = 0.26$ for progenitors in the mass range of 10–40 $M_\odot$ in order to phenomenologically include the dependence of the SN explosion on progenitor in this mass range. We then take $f_{\rm fSN} = 1.00$ for $M > 40\ M_\odot$. We use this SN-progenitor relationship as the fiducial case throughout this work. For comparison, we also apply $f_{\rm fSN} = 1.00$ for $M > 18\ M_\odot$, which has been adopted in previous work with respect to the red supergiant problem (Hidaka et al. 2016).

3. Cosmic Star Formation Rate

Several different SFR formulae have been proposed to fit the observational data. The data mostly are interpreted from the UV luminosity of galaxies at different redshifts (e.g., Bouwens et al. 2012; Cucciati et al. 2012). This derivation is complicated because of the possible extinction due to the dust surrounding galaxies (Buat et al. 2012). Also, the stellar composition at different ages must be taken into consideration so that the color of each galaxy is matched to the observations (Conroy 2013).

Typically a Salpeter-like IMF is assumed for both the deduction of the SFR from the UV light and the color matching. Moreover, not only the UV source but also the IR emission is used for the SFR estimate (Magnelli et al. 2011; Gruppioni et al. 2013).

The relic supernova neutrino spectrum depends strongly upon the SFR through the rate of occurrence for each type of SN. In this work, we adopt the SFR fitting formula proposed by Madau & Dickinson (2014; see Figure 1) given by

$$\Psi_*(z) = \frac{a(1+z)^b}{1+[(1+z)/d]^c}\, M_\odot\ \mathrm{year}^{-1}\,\mathrm{Mpc}^{-3}, \qquad (1)$$

where $a = 0.015$, $b = 2.7$, $c = 5.6$, and $d = 2.9$. It has been argued (Horiuchi et al. 2011) that the observationally deduced supernova rate tends to be smaller than the theoretical value. This is the so-called supernova rate problem (Horiuchi et al. 2011; Mathews et al. 2014). This depends upon the choice of SFR. The SFR adopted in this work gives a more conservative relic SN neutrino estimation and is independent of the supernova rate problem (Madau & Dickinson 2014).

As mentioned above, most evaluations of the SFR are based upon the UV luminosity, which is mainly emitted by OB stars. The dust surrounding galaxies, however, always complicate the evaluation of the UV. There is a claim (Rowan-Robinson et al. 2016) that the SFR based upon UV light is an underestimate especially for starburst galaxies. Recently, a new method based upon SED modeling has been proposed (Rowan-Robinson et al. 2016) in order to take into account the star formation embedded in dense molecular clouds. This study has shown that the SFR for $z > 3.5$ is higher by a factor of two to three than the estimate from UV light. We also apply this SFR to see how it affects the relic SN neutrino spectrum compared to the fiducial case.

4. IMF: Universal or Variable

The IMF is commonly assumed to be a universal function that is independent of the physical conditions of the star formation site. One of the popular functional forms is the Salpeter-A IMF (Sal-A; Baldry & Glazebrook 2003). This is a two-segment power law given by

$$\phi_0(M) = M^{-\zeta} = M^{-(1+\Gamma)} \qquad (2)$$

with $\zeta = 2.35 \pm 0.2$ ($\Gamma = 1.35 \pm 0.2$) for stars with $M \geqslant 0.5 M_\odot$ and $\zeta = 1.5$ ($\Gamma = 0.5$) for stars with $0.1 < M < 0.5 M_\odot$. This is the adopted IMF for the present work. Most of the popular IMFs including the Sal-A are observationally deduced for stars in the Milky Way. There are also theoretical derivations of the power-law index for the IMF. For example, a power-law IMF is explained by the turbulent motion of molecular clouds in a magnetic field (Padoan & Nordlund 2002). There is, however, no definitive theory for the IMF, and the universality of the IMF remains an open question.

The relationship between metallicity and the IMF also needs to be considered (Hoversten & Glazebrook 2008; Meurer et al. 2009; Gunawardhana et al. 2011; Conroy & van Dokkum 2012). It has been postulated that the IMF in metal-poor environments could be top-heavy. This is because molecular clouds in that condition may not sufficiently cool to allow them to collapse gravitationally on small scales, even though dust may help as a coolant (Dopcke et al. 2013). Nevertheless, a metallicity-dependent variable IMF is worth investigating regarding its effect on the relic supernova neutrino spectrum. We explore the IMF–metallicity relationship by adopting a cosmological metallicity evolution in Section 6.4. If we consider a variable IMF, it is necessary to make a correction to the SFR, which is IMF dependent. We describe this in Section 5.2.

5. Relic Supernova Neutrino Spectrum

In this section, we summarize the scheme with which the neutrino signals are evaluated. In addition to the basic formulae, we briefly show how to modify the SFR depending upon the choice of IMF and also include neutrino oscillations.

5.1. Basic Formulae

We follow the standard method to evaluate the detection rate of relic SN neutrinos as described in paper II (see also Strigari et al. 2005; Lunardini (2006); Yüksel & Beacom 2007). For each type of SN, the neutrino number flux per unit energy is

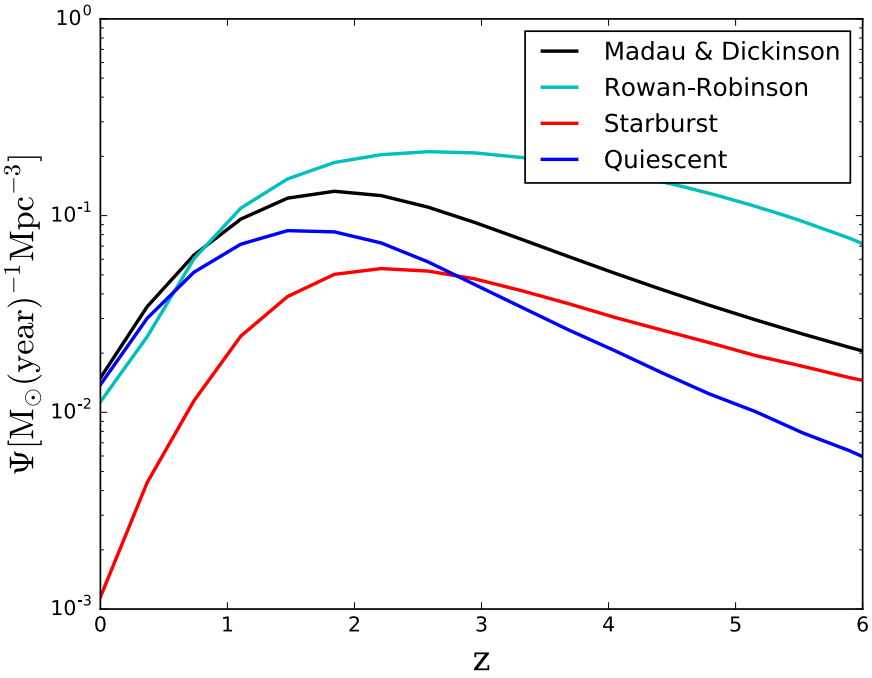

Figure 1. (Color online) Star formation rates adopted in this work. Black line shows the SFR by Madau & Dickinson (2014) that is taken as the fiducial case. The cyan line shows the SFR by Rowan-Robinson et al. (2016). The figure also includes starburst (red) and quiescent (blue) components suggested by Lacey et al. (2016).

determined by

$$\frac{dN_\nu}{dE_\nu} = \frac{c}{H_0}\int_0^{z_{\max}} R_{\rm SN}(z)\frac{dN_\nu(E'_\nu)}{dE'_\nu} \times \frac{dz}{\sqrt{\Omega_m(1+z)^3+\Omega_\Lambda}}, \quad (3)$$

where we adopt $z_{\max} = 5$ as the redshift at which star formation begins and $R_{\rm SN}$ is the cosmic supernova rate. $dN_\nu(E'_\nu)/dE'_\nu$ is the neutrino spectrum emitted at the source, and the energy $E'_\nu = (1+z)E_\nu$ is the energy at emission. E_ν is the redshifted energy observed in the detector. A standard cosmology with $H_0 = 70$ km s^{-1} Mpc^{-1}, $\Omega_m = 0.3$, $\Omega_\Lambda = 0.7$ (Horiuchi et al. 2011; Hinshaw et al. 2013) is adopted. We assume a Fermi–Dirac distribution for all neutrino species from each type of SN. These are parameterized by the effective neutrino temperature and the total energy of emitted neutrinos as summarized in Table 1.

Two models of fSNe, one with a soft EoS (LS-EoS, $K = 180$; Lattimer & Swesty 1991) and one with a stiff EoS (Shen-EoS, Shen et al. 1998) are included by adopting the numerical models of Sumiyoshi et al. (2008).

The supernova rate $R_{\rm SN}$ is then given by

$$R_{\rm SN}(z) = \Psi_*(z) \times \frac{\int_{M_{\rm SN}} dM\ \phi_0(M)}{\int_{M_{\min}}^{M_{\max}} dM\ M\phi_0(M)}, \quad (4)$$

where $\Psi_*(z)$ is the cosmic SFR, and $\phi_0(M)$ is the IMF. Here, $M_{\rm SN}$ denotes the range of progenitor masses that lead to a particular type of SN. Hence, it is obvious that the neutrino flux depends not only upon the cosmic SFR and the IMF, but also upon the occurrence of each type of SN. Here, we assume $M_{\min} = 0.1M_\odot$ and $M_{\max} = 125M_\odot$.

Table 1
Parameters for the Various Neutrino Sources Considered in This Work

Detail	ONeMg	CCSNe (optically luminous)	fSNe (Shen EoS)	fSNe (LS EoS)
Mass ($M_\odot$)	8–10	10–40 (74%)	10–40 (26%), 40–125	10–40 (26%), 40–125
T_{ν_e}(MeV)	3.0 ± 0.3	3.2 ± 0.32	7.25 ± 0.73	5.58 ± 0.56
$T_{\bar\nu_e}$(MeV)	3.6 ± 0.36	4.0 ± 0.50	8.25 ± 0.83	6.67 ± 0.67
T_{ν_x}(MeV)	3.6 ± 0.36	6.0 ± 0.60	9.27 ± 0.93	8.22 ± 0.82
$E_{\nu_e}^{\rm total}$(erg)	3.3×10^{52}	5.0×10^{52}	13.5×10^{52}	4.4×10^{52}
$E_{\bar\nu_e}^{\rm total}$(erg)	2.7×10^{52}	5.0×10^{52}	12.7×10^{52}	3.7×10^{52}
$E_{\nu_x}^{\rm total}$(erg)	1.1×10^{52}	5.0×10^{52}	5.3×10^{52}	1.9×10^{52}

Notes.
[a] Values for luminous SNe are from Mathews et al. (2014) and those for fSNe are derived from the T50 models in Sumiyoshi et al. (2008).
[b] Temperature uncertainty estimated from the time variation of neutrino temperatures during the first few seconds.

Then, the detector event rate is

$$\frac{dN_{\rm event}}{dE_{e^+}} = N_{\rm target}\frac{1}{c}\frac{dN_\nu}{dE_\nu}\sigma(E_\nu)\frac{dE_\nu}{dE_{e^+}}, \quad (5)$$

where $N_{\rm target}$ is the number of target particles in the detector. $\sigma(E_\nu)$ is the cross section for neutrino interactions within the detector (Strumia & Vissani 2003). In the following calculations, we assume a water Čerenkov detector so that the neutrino absorption is dominated by the $\bar\nu_e + p \rightarrow e^+ + n$ reaction with $E_\nu = E_{e^+} + 1.3$ MeV.

5.2. Relationship between the SFR and the IMF

In Section 6, we will show the results obtained by adopting different scenarios, i.e., different versions of the SFR, the IMF,

and the SN occurrence. We then evaluate the EoS dependence of the relic SN neutrino spectrum for each case.

If we use an IMF that is different from that used for the SFR evaluation, we need to introduce an overall scaling factor for the cosmic SFR. For example, this is the case when we apply a metallicity-dependent IMF. The scaling factor is estimated by assuming that the observational cosmic SFR correctly gives the UV luminosity from a galaxy. We also suppose that the UV light is emitted by OB stars, the masses of which range from $M_{\rm B0} \approx 15 M_\odot$ to $M_{\rm O5} \approx 40 M_\odot$. Then, the SFR Ψ is given by

$$\Psi \times \tau_{\rm O5} = N_0 \times \int_{M_{\rm min}}^{M_{\rm max}} M\phi(M) dM, \quad (6)$$

where $\tau_{\rm O5}$ is the lifetime of an O5 star, and N_0 is a normalization constant. A constant SFR over the lifetime of OB stars is assumed. The total UV luminosity is similarly obtained by

$$L_{\rm UV}^{\rm tot} = N_0 \times \int_{M_{\rm B0}}^{M_{\rm O5}} L_{\rm UV}(M)\phi(M) dM, \quad (7)$$

where $L_{\rm UV}(M)$ is the UV luminosity emitted by a star of mass M. According to these equations, the transformation from an SFR based upon an IMF ϕ_0 to an SFR based upon a different IMF ϕ_1 is given by

$$\Psi_1 = \frac{\int_{M_{\rm min}}^{M_{\rm max}} M\phi_1(M) dM}{\int_{M_{\rm B0}}^{M_{\rm O5}} L_{\rm UV}(M)\phi_1(M) dM} \times \frac{\int_{M_{\rm B0}}^{M_{\rm O5}} L_{\rm UV}(M)\phi_0(M) dM}{\int_{M_{\rm min}}^{M_{\rm max}} M\phi_0(M) dM} \times \Psi_0, \quad (8)$$

where Ψ_0 and Ψ_1 denote SFRs with IMF ϕ_0 and ϕ_1, respectively.

We can evaluate $L_{\rm UV}(M)$ by assuming $L_{\rm tot} \propto T_{\rm eff}^6$, which is an empirical fitting formula for main-sequence stars on the HR-diagram, and a mass–luminosity relation, $L_{\rm tot} \propto M^{3.5}$ (see Demircan & Kahraman 1991). $T_{\rm eff}$ is the effective surface temperature of the star. We also assume a blackbody spectrum to estimate the UV luminosity by taking $\lambda_{\rm UV} = 91$–280 nm. This scheme is applied whenever we use an IMF that is not the same as that employed to deduce the SFR from the observations.

5.3. Neutrino Oscillations

We also consider the effects of neutrino oscillations on the final neutrino signals. Two possible cases were considered in Paper II (see also Dighe & Smirnov 2000), i.e., either a normal or inverted mass hierarchy associated with complete non-adiabatic mixing (Case I) and an inverted mass hierarchy associated with complete adiabatic mixing (Case II) through the MSW high-density resonance. We denote the case without neutrino oscillations as Case III.

In Case I, the neutrino flux would be

$$\phi_{\bar{\nu}_e} = 0.7 \times \phi^0_{\bar{\nu}_0} + 0.3 \times \phi^0_{\bar{\nu}_x}, \quad (9)$$

while in Case II, by ignoring the effect from shock wave propagation that may induce a non-adiabatic transition, the flux would be

$$\phi_{\bar{\nu}_e} = \phi^0_{\bar{\nu}_x}. \quad (10)$$

We apply these schemes to each different astronomical scenario.

6. Results

We numerically treat both Type-II SNe and SNeIb,c as luminous core-collapse SNe in the same manner and denote them simply as CCSNe. We then show the results within different astrophysical scenarios. For each case, we consider the neutrino oscillations (Cases I&II). In the following subsections, we first present the cases without neutrino oscillations (Case III).

The cases with neutrino oscillation are shown at the end of this section. The overall shape of the neutrino spectra are similar to each other for all cases. However, we note that the EoS dependence appears as a robust separation between the predicted RSN spectra for a stiff versus a soft EoS as discussed below.

6.1. Fiducial Case: Without Neutrino Oscillations

First we consider the fiducial case as follows. We adopt the SFR parameterized by Madau & Dickinson (2014) including their the upper and lower 1σ limits. A Salpeter-A IMF is chosen as the universal IMF. We also consider 8–$10 M_\odot$ progenitor stars to be ONeMg SNe. As mentioned in Section 2, we adopt a non-monotonic dependence of CCSNe or fSN for progenitors in the mass range of 10–40 $M_\odot$: i.e., 74% of 10–$40 M_\odot$ progenitor stars become CCSNe; while 26% of 10–$40 M_\odot$ progenitor stars become fSNe. All progenitors with $M > 40 M_\odot$ are taken to result in fSNe. The neutrino energy spectrum and the total energy emitted by each type of SN are parameterized by Fermi–Dirac distributions and summarized in Table 1.

We adopt the results of the numerical study by Hüdepohl et al. (2010) for the ONeMg SNe. We also accept the values for CCSNe from the comprehensive study of SN 1987A by Vissani (2015). The numerical study by Sumiyoshi et al. (2008) provides the time evolution of the luminosity L_ν and the averaged energy $\langle E_\nu \rangle$ for fSNe based upon two EoSs, Lattimer–Swesty and Shen EoS. The total energy spectrum is obtained by integrating the luminosity over time. We fit the spectrum with a Fermi–Dirac distribution to estimate the effective temperature of neutrinos.

Figure 2 shows results without neutrino oscillations (Case III). These results manifest the EoS dependence mainly in the high-energy tail of the spectrum around $E_{e^+} = 30$–40 MeV. This is where the neutrino signals begin to overwhelm the atmospheric neutrino background. We indicate this location by a rectangle denoting the uncertainty bounds due to the SFR. These rectangular regions for the Shen and LS EoSs are well separated from each other. Similarly, we also place another rectangle around the peak of the neutrino spectrum. In the following, we use these regions to characterize the spectra for the different astronomical scenarios. In this figure, we also include results based upon the original neutrino spectrum by Sumiyoshi et al. (2008). The difference is small, and the Fermi–Dirac distribution is good enough for our study.

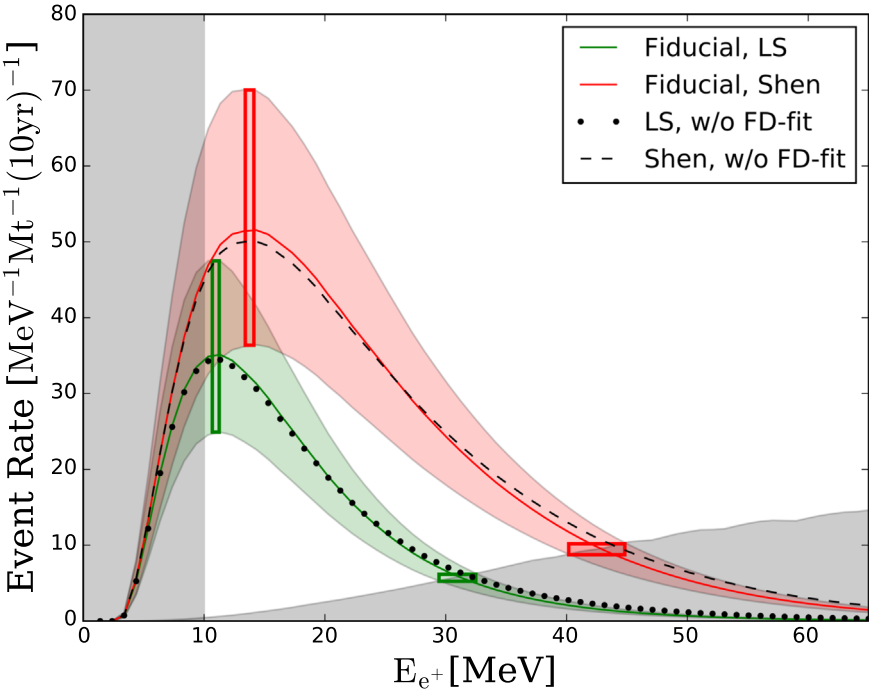

Figure 2. Predicted e^+ energy spectra and uncertainties in the total RSN detections for the fiducial case. SFR by Madau & Dickinson (2014) is used, and the sporadic SN occurrence of Pejcha & Thompson (2015) is adopted. No neutrino oscillations are considered (Case III). The uncertainty bands are based upon the observed cosmic SFR and the detector statistics. The results for two different fSNe models based upon the stiff EoS of Shen et al. (1998) and the soft EoS of Lattimer & Swesty (1991) are included. The cases based upon the original numerical data by Sumiyoshi et al. (2008) are also included as dotted and dashed lines. The shaded energy range below 10 MeV indicates the region where the background noise due to reactor $\bar{\nu}_e$ may dominate. The shaded energy range that intersects the spectrum at ∼30–46 MeV indicates the region where the background may be dominated by noise from atmospheric neutrinos. Rectangular regions represent the peak of the spectrum and the locations where the neutrino signals overwhelm the atmospheric neutrino noise.

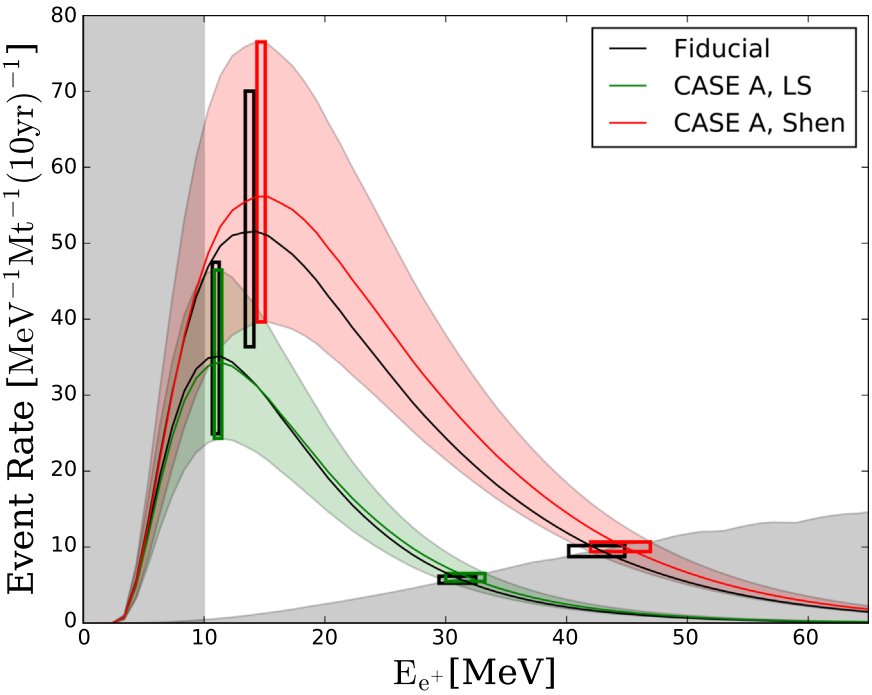

Figure 3. Same as Figure 2 but for Case A including the RSG problem. The results for the fiducial cases (without the error bands) are also included in black.

6.2. Case A: RSG Problem Motivated

We investigate the the same case as in Paper II with the SFR of Madau & Dickinson (2014). We considered 8–10$M_\odot$ progenitor stars to be ONeMg SNe, 10–18$M_\odot$ progenitor stars to be CCSNe. As suggested by the red supergiant problem, progenitor stars with 18–125$M_\odot$ are taken to be fSNe that are too dim to be detected optically. The results are shown in Figure 3. We note that the EoS dependence is robust just as in the fiducial cases. The rectangular regions in the high-energy

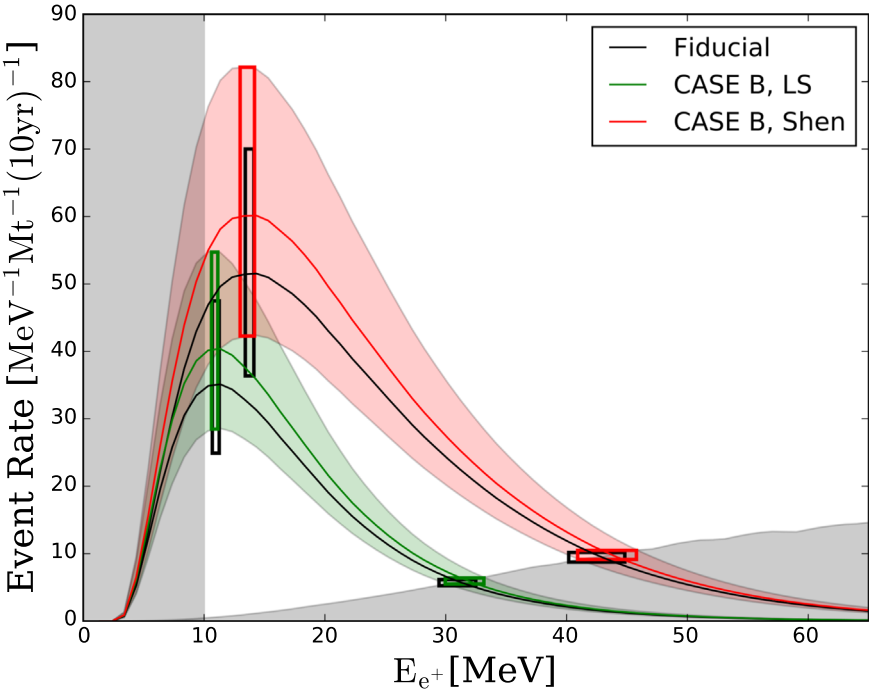

Figure 4. Same as Figure 2 but for Case B including starburst and quiescent star formation. The results for the fiducial cases (without the error bands) are also included in black.

tail, which characterize the EoS dependence, are well separated and overlap those for the fiducial cases.

6.3. Case B: Starburst and Quiescent SFR

It has been speculated that star formation occurs in two phases, either via starbursts or in a quiescent phase. In general, the starburst star formation is triggered by a major merger, while late spiral galaxies like the Milky Way form stars in a quiescent phase.

Recent cosmological large-scale simulations can trace the star formation history from the early universe at high-z. Lacey et al. (2016) made self-consistent simulations leading to a direct comparison with the observational quantities. They were able to identify these two star formation phases. It was noticed that the starburst phase dominates at high-z, while quiescent star formation becomes dominant later in cosmic history (see Figure 1). Moreover, they found that in order to recover the SFR of Madau & Dickinson (2014), it is necessary to apply a different IMF for the starburst and quiescent star formation phase. That is, they use a top-heavy IMF for the starbursts instead of using the same standard IMF for both star formation phases.

As mentioned in the Introduction, this finding is physically reasonable. Metals work as coolants and cause the molecular cloud to be fragmented onto smaller scales. Hence, stars that formed in metal-poor conditions tend to be more massive, leading to a top-heavy IMF.

It is, however, not so straightforward to determine the relationship between the IMF and metallicity. In addition to metals, dust also acts as a coolant, and the early supernovae distribute the dust quite efficiently into the interstellar medium. Although this could be a possibility, our purpose in this work is to examine the EoS dependence in a wide variety of circumstances, and it is worthwhile to investigate scenarios with a different IMF for each star formation phase. We take the fraction of each type of star formation phase from their result, and apply the $\mathrm{IMF_{SB}}$ and $\mathrm{IMF_{Q}}$ to the starburst and quiescent phase, respectively, by taking $\Gamma_{\mathrm{SB}} = 1.0$ and $\Gamma_{\mathrm{Q}} = 1.35$ for Equation (2). The results are shown in Figure 4 along with the fiducial case. The EoS dependence is indicated by the rectangular regions in the high-energy tail. These remain similar to the two cases mentioned above as indicated.

6.4. Case C: Metallicity-dependent Variable IMF

Two different IMFs were applied in the previous case. These can be considered as examples of a metallicity-dependent IMF. These reflect the metallicity dependence since the starburst phase is dominant at high-z. Thus, a metal-poor environment could occur. If we consider more realistic cosmic chemical evolution, the metallicity increases continuously, and the IMF also should change gradually according to the chemical enrichment of the interstellar medium.

There is observational evidence that this continuous IMF evolution exists in low-z galaxies. Martín-Navarro et al. (2016) found a clear IMF–metallicity relationship given by

$$\Gamma = 2.2(\pm 0.1) + 3.1(\pm 0.5) \times [M/\mathrm{H}]. \quad (11)$$

Metallicity evolution is closely related with galaxy evolution. However, both the stellar and gas-phase metallicity must be accurately considered. Ma et al. (2016) recently studied the galaxy mass–metallicity relation based upon cosmological zoom-in simulations that include gas inflow and outflow to estimate the metallicity evolution accurately. They found $[M/\mathrm{H}] = 0.4[\log(M_*/M_\odot) - 10] + 0.67\exp(-0.50z) - 1.04$, where M_* is the galactic stellar mass. For the metallicity of the gas phase, it was found that $[M/\mathrm{H}] = 0.35[\log(M_*/M_\odot) - 10] + 0.93\exp(-0.43z) - 1.05$. In addition, galactic mass evolution is expected, and the average of M_* depends upon the redshift z. The galaxy cosmological mass function can be expressed $\langle M_* \rangle = 10^{11}(1+z)^{-0.58}[M_\odot]$ (Lopes et al. 2014). These two studies can be used to deduce the cosmic metallicity evolution for each component as shown in Figure 5. By combining the

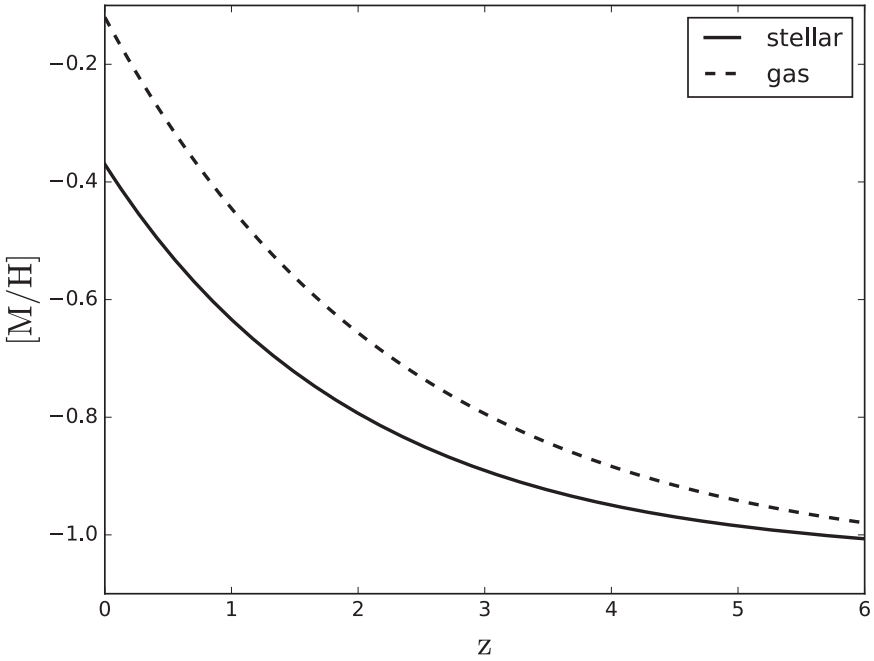

Figure 5. Metallicity–redshift relationship. The mass–metallicity relationship by Ma et al. (2016) and the Galaxy Mass Function by Lopes et al. (2014) are adopted to derive this cosmic metallicity evolution. Solid and dashed lines represent the stellar and gas-phase metallicity, respectively.

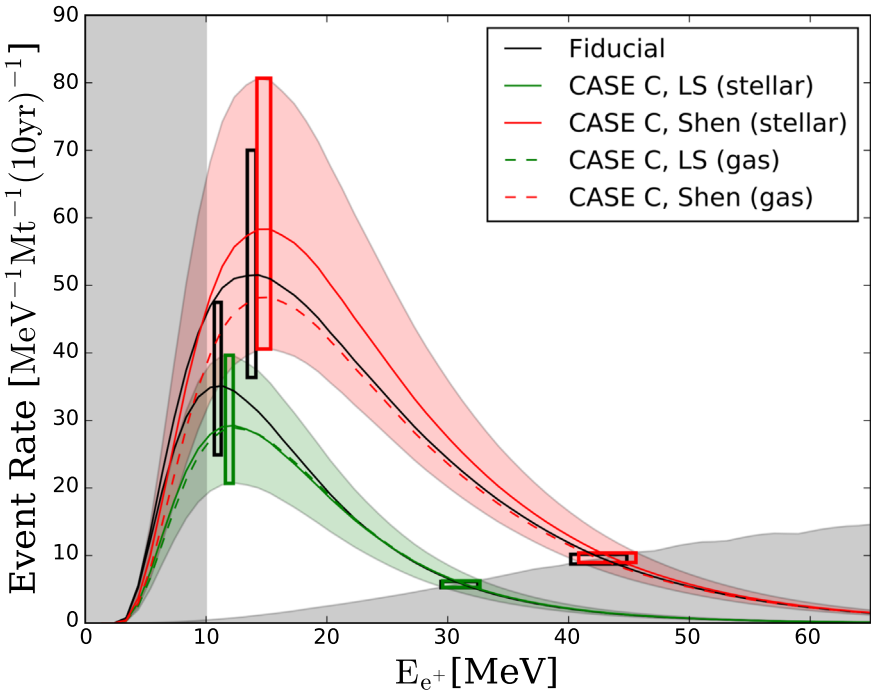

Figure 6. Same as Figure 2 but for Case C including a metallicity-dependent IMF. Solid lines with uncertainty band are for the cases with the stellar metallicity evolution. Dashed lines are for the cases with the gas-phase metallicity evolution (see details in the text). The results for the fiducial cases (without the error bands) are also included in black.

IMF–metallicity relationship (11) with the cosmic metallicity evolution, we can apply a z-dependent IMF along with the SFR to evaluate the relic SN neutrino spectrum. As described in Section 5.2, we also make a correction to the SFR given by Madau & Dickinson (2014). We then calculate the relic SN neutrino spectrum. The results are shown in Figure 6. This figure also includes the fiducial case. It reveals a very similar EoS dependence for the RSN spectrum.

6.5. Case D: SFR Enhanced at High-z

So far we have used the SFR by Madau & Dickinson (2014). However, a recent study (Rowan-Robinson et al. 2016) has shown the possibility that the SFR evaluation via UV data underestimates the contribution from stars embedded inside dust, especially for starburst galaxies at high-z. This new analysis gives a higher SFR for $z > 4$ (see Figure 1). Hence, in addition to the absolute value of the SFR, the

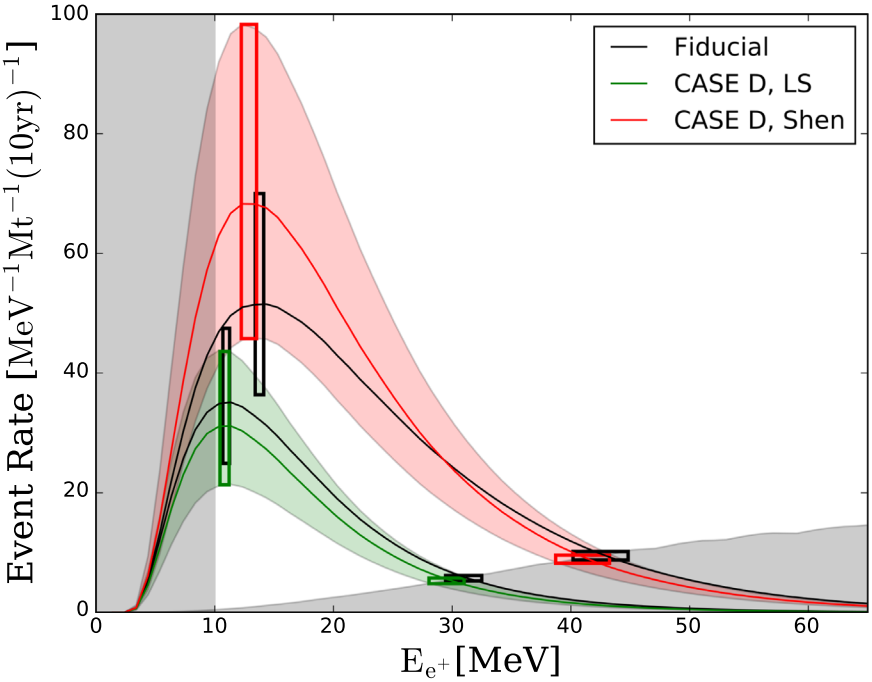

Figure 7. Same as Figure 2 but for Case D including an enhanced SFR at high redshift. The results for the fiducial cases (without the error bands) are also included in black.

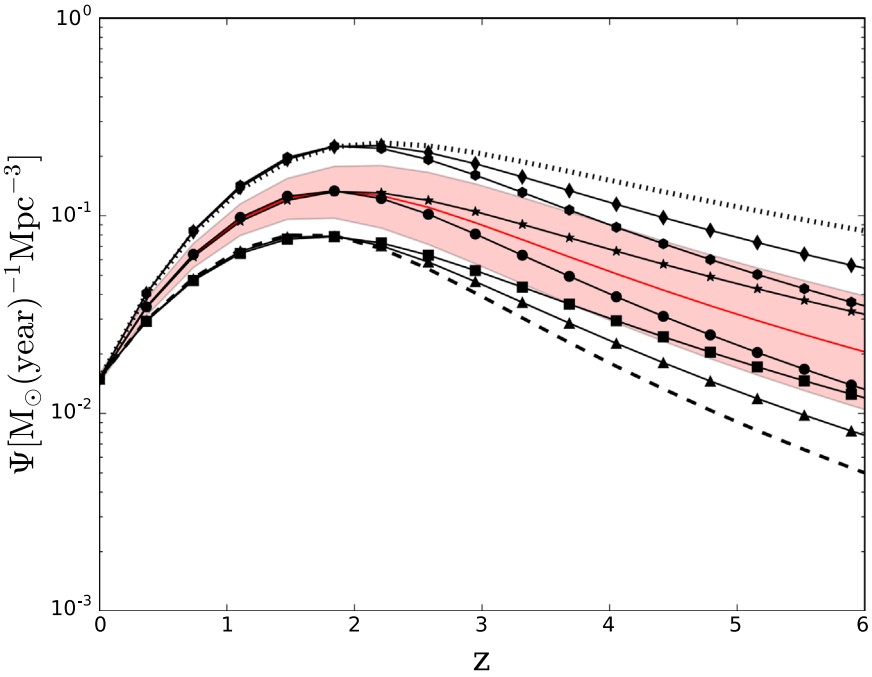

Figure 8. Variations of SFR based upon the SFR by Madau & Dickinson (2014). The case of the original parameters is shown in red line with the red shaded uncertainty. Variations are made by combination of $b = 2.7 \pm 0.5$ and $c = 5.6 \pm 0.5$ in Equation (3). They are: $(b, c) = (2.7 + 0.5, 5.6)$ (diamonds), $(b, c) = (2.7 - 0.5, 5.6)$ (triangles), $(b, c) = (2.7, 5.6 + 0.5)$ (circles), $(b, c) = (2.7, 5.6 - 0.5)$ (stars), $(b, c) = (2.7 + 0.5, 5.6 + 0.5)$ (hexagons), $(b, c) = (2.7 - 0.5, 5.6 - 0.5)$ (squares). The largest downward and upward deviation corresponds to $(b, c) = (2.7 - 0.5, 5.6 + 0.5)$ (dashed line) and $(b, c) = (2.7 + 0.5, 5.6 - 0.5)$ (dotted line), respectively.

metallicity-dependent IMF can also affect the relic SN neutrino spectrum. Here, we adopt this SFR along with the same variable IMF as in the previous subsection. The results are shown in Figure 7. Even in this case, one can discern the EoS dependence in the high-energy tail of the spectrum, although the peak height increases due to the enhanced SFR.

It is interesting to see how in general the shape of the SFR influences the neutrino energy spectrum, especially the EoS dependency. In order to see this, we choose variations of the SFR by taking different parameter sets (b, c) of Equation (3). These are shown in Figure 8. The RSN spectrum for the two extreme cases of $(b, c) = (2.7 - 0.5, 5.6 + 0.5)$ (dashed line)

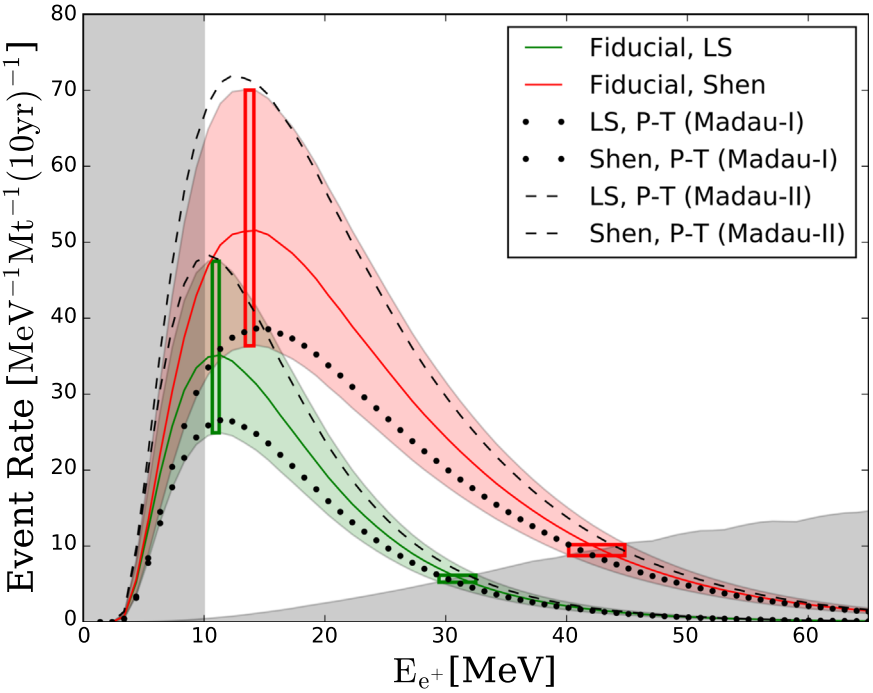

Figure 9. Same as Figure 2 but including cases of modified SFR with $(b, c) = (2.7 - 0.5, 5.6 + 0.5)$ (Madau-II) and $(b, c) = (2.7 + 0.5, 5.6 - 0.5)$ (Madau-I) in Equation (3) for each EoS.

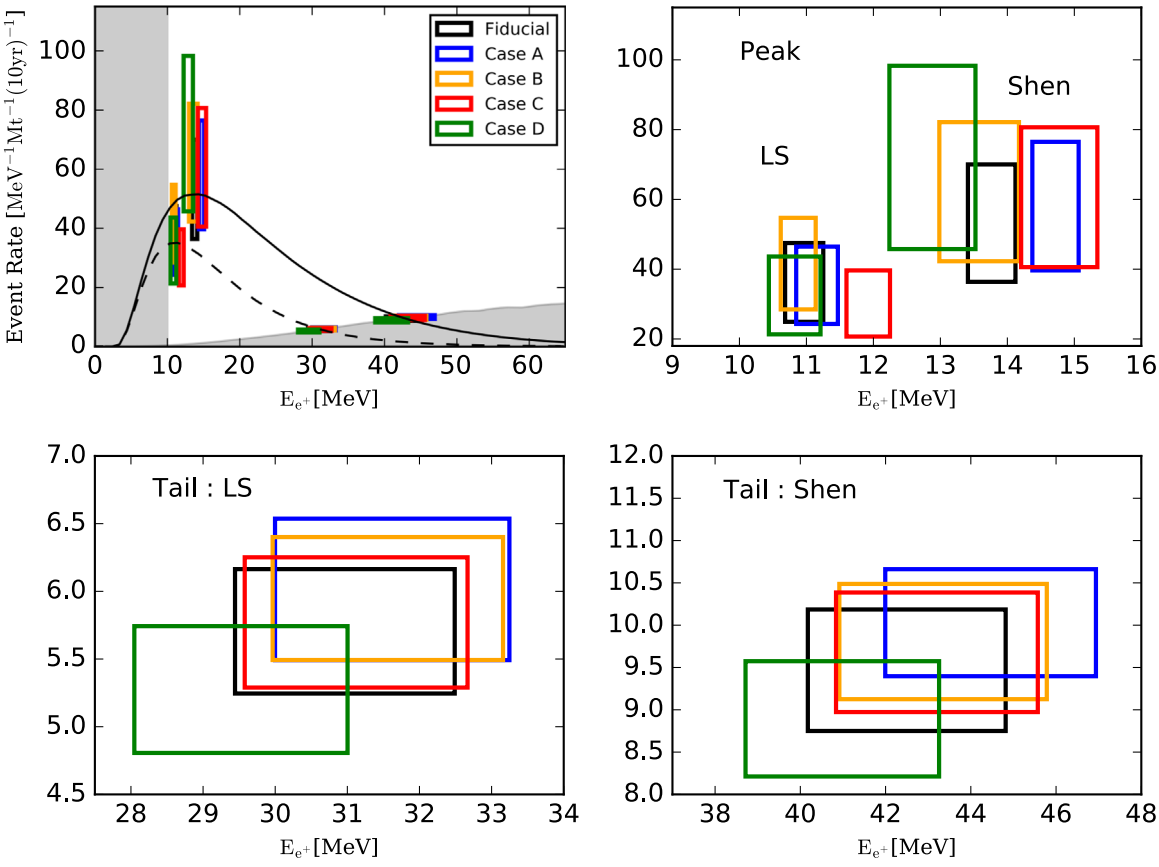

Figure 10. Comparison of Case III (without neutrino oscillation) for all scenarios: fiducial, Case A, B, C, and D. The figure includes only rectangles for the location of peak and tail, which characterize the spectrum for each cases. In the left upper panel, the spectrum of the fiducial case without the error band are included for reference. The solid line is for the Shen EoS and the dashed line for the LS EoS. The right upper panel shows the detail of the peak locations for both the Shen and LS EoSs. Similarly the details of tails are shown in the left bottom (for the LS EoS) and right bottom panel (for the Shen EoS).

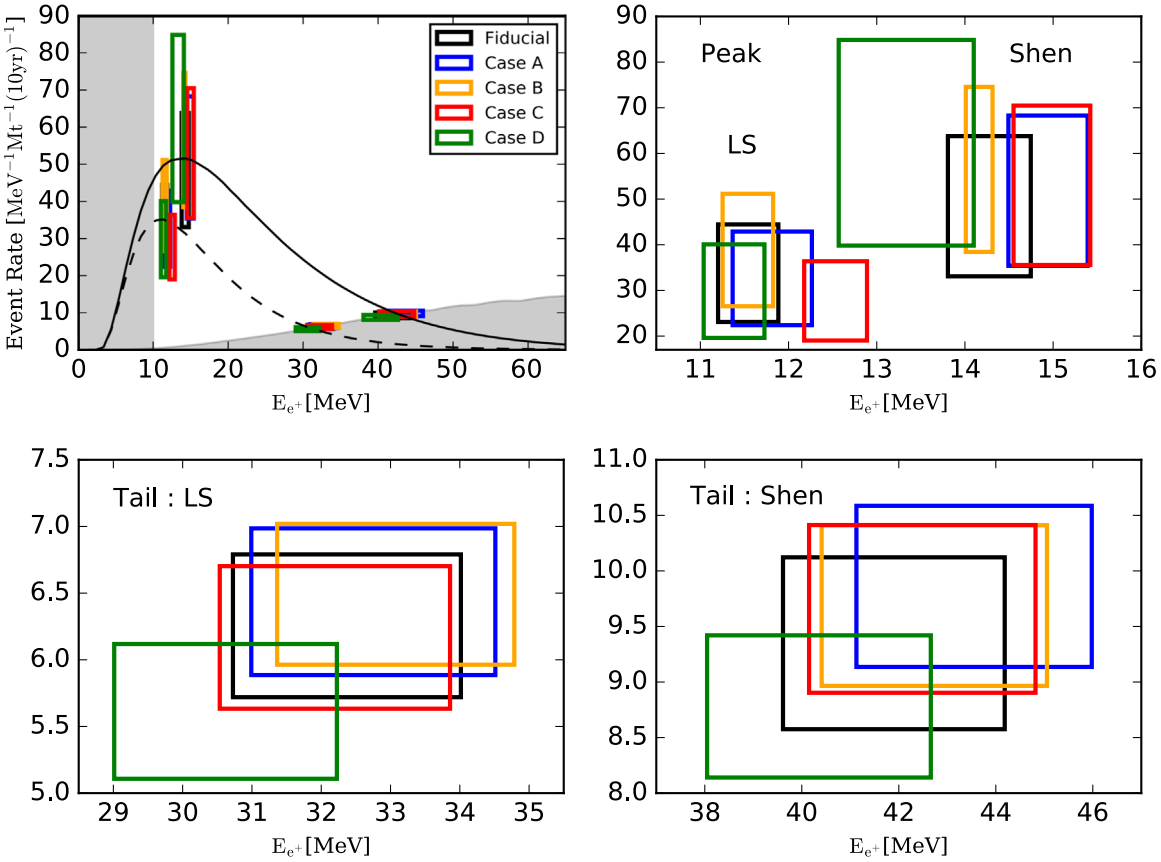

Figure 11. Same as Figure 10 but for Case I, complete non-adiabatic mixing.

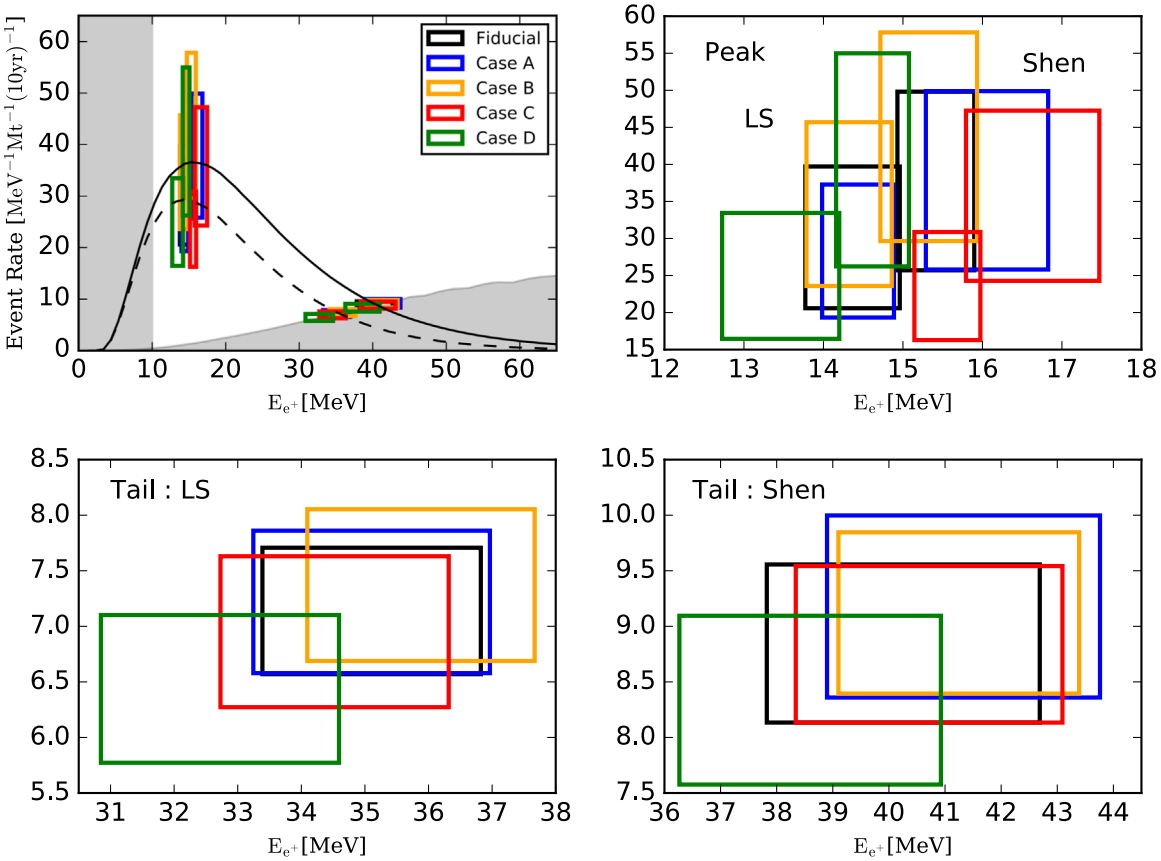

Figure 12. Same as Figure 10 but for Case II, complete adiabatic mixing.

and $(b, c) = (2.7 + 0.5, 5.6 - 0.5)$ (dotted line) are shown in Figure 9. While these modified SFRs significantly deviate from the fiducial SFR, the EoS dependence in the RSN spectrum are not affected. This is consistent with the case shown in Figure 7.

6.6. Comparison among the Different Astrophysical Scenarios

Figure 10 shows the result of all instances of Case III. This figure reveals the robustness of the EoS dependence by indicating the characteristic locations with the rectangular symbols as described above. We note that the EoS dependence appears as a robust separation between the predicted RSN spectra for a stiff versus a soft EoS.

6.7. Neutrino Oscillations

Up to now, we have only considered cases without neutrino oscillations, i.e., $\bar{\nu}_e^0 \rightarrow \bar{\nu}_e$ (Case III). In this subsection, we take into account neutrino oscillations in either the normal or inverted mass hierarchies for all cases described in the previous subsections. We follow the mixing scheme described in Section 5.3 (Case I & II). The results are shown in Figure 11 (Case I) and Figure 12 (Case II). In this figure, the robustness of the EoS dependence is clearly seen just as in the cases without neutrino oscillations. However, it is slightly weaker for the case of the inverted mass hierarchy, i.e., the separation of the rectangular regions for the Shen and LS EoS is slightly less.

7. Conclusion

As the fiducial case in this study, we have adopted the SFR parameterized by Madau & Dickinson (2014) along with the sporadic CCSN/fSN occurrence in the mass range of 10–40$M_\odot$ based upon the numerical studies of Pejcha & Thompson (2015). We then estimated the RSN spectrum. In addition, we have considered a wide variety of astrophysical scenarios and investigated the EoS dependence of the RSN spectrum for each case with and without the occurrence of neutrino oscillations. We find that the EoS dependence of the RSN spectrum manifests prominently in the high-energy tail in any scenario considered. The robustness of this EoS dependence can be understood in that the RSN spectrum is determined mostly by the SFR for $z < 2$. For example, in the case D, which adopts an enhanced cosmic SFR for $z > 3$, it is clearly seen that the RSN exhibits an EoS dependence similar to that of the fiducial cosmic SFR.

This work was supported in part by Grants-in-Aid for Scientific Research of JSPS (26105517, 24340060) of the Ministry of Education, Culture, Sports, Science and Technology of Japan. Work at the University of Notre Dame (G.J.M.) was supported by the U.S. Department of Energy under Nuclear Theory Grant DE-FG02-95-ER40934.

ORCID iDs

G. J. Mathews https://orcid.org/0000-0002-2663-0540

References

Baldry, I. K., & Glazebrook, K. 2003, ApJ, 593, 258
Bouwens, R. J., Illingworth, G. D., Oesch, P. A., et al. 2012, ApJL, 752, L5
Buat, V., Noll, S., Burgarella, D., et al. 2012, A&A, 545, A141
Conroy, C. 2013, ARA&A, 51, 393
Conroy, C., & van Dokkum, P. G. 2012, ApJ, 760, 71
Cucciati, O., Tresse, L., Ilbert, O., et al. 2012, A&A, 539, A31
Demircan, O., & Kahraman, G. 1991, Ap&SS, 181, 313
Dighe, A. S., & Smirnov, A. Y. 2000, PhRvD, 62, 033007
Dopcke, G., Glover, S. C. O., Clark, P. C., & Klessen, R. S. 2013, ApJ, 766, 103
Ertl, T., Janka, H.-T., Woosley, S. E., Sukhbold, T., & Ugliano, M. 2016, ApJ, 818, 124
Gruppioni, C., Pozzi, F., Rodighiero, G., et al. 2013, MNRAS, 432, 23
Gunawardhana, M. L. P., Hopkins, A. M., Sharp, R. G., et al. 2011, MNRAS, 415, 1647
Hidaka, J., Kajino, T., & Mathews, G. J. 2016, ApJ, 827, 85
Hinshaw, G., Larson, D., Komatsu, E., et al. 2013, ApJS, 208, 19
Horiuchi, S., Beacom, J. F., & Dwek, E. 2009, PhRvD, 79, 083013
Horiuchi, S., Beacom, J. F., Kochanek, C. S., et al. 2011, ApJ, 738, 154
Horiuchi, S., Nakamura, K., Takiwaki, T., Kotake, K., & Tanaka, M. 2014, MNRAS, 445, L99
Hoversten, E. A., & Glazebrook, K. 2008, ApJ, 675, 163
Hüdepohl, L., Müller, B., Janka, H.-T., Marek, A., & Raffelt, G. G. 2010, PhRvL, 104, 251101
Keehn, J. G., & Lunardini, C. 2012, PhRvD, 85, 043011
Lacey, C. G., Baugh, C. M., Frenk, C. S., et al. 2016, MNRAS, 462, 3854
Lattimer, J. M., & Swesty, D. F. 1991, NuPhA, 535, 331
Lentz, E. J., Bruenn, S. W., Hix, W. R., et al. 2015, ApJL, 807, L31
Lopes, A. R., Iribarrem, A., Ribeiro, M. B., & Stoeger, W. R. 2014, A&A, 572, A27
Lunardini, C. 2006, APh, 26, 190
Ma, X., Hopkins, P. F., Faucher-Giguère, C.-A., et al. 2016, MNRAS, 456, 2140
Madau, P., & Dickinson, M. 2014, ARA&A, 52, 415
Magnelli, B., Elbaz, D., Chary, R. R., et al. 2011, A&A, 528, A35
Martín-Navarro, I., Brodie, J. P., van den Bosch, R. C. E., Romanowsky, A. J., & Forbes, D. A. 2016, ApJL, 832, L11
Mathews, G. J., Hidaka, J., Kajino, T., & Suzuki, J. 2014, ApJ, 790, 115
Melson, T., Janka, H.-T., Bollig, R., et al. 2015a, ApJL, 808, L42
Melson, T., Janka, H.-T., & Marek, A. 2015b, ApJL, 801, L24
Meurer, G. R., Wong, O. I., Kim, J. H., et al. 2009, ApJ, 695, 765
Müller, B. 2015, MNRAS, 453, 287
Nakamura, K., Takiwaki, T., Kuroda, T., & Kotake, K. 2015, PASJ, 67, 107
O'Connor, E., & Ott, C. D. 2011, ApJ, 730, 70
Padoan, P., & Nordlund, Å. 2002, ApJ, 576, 870
Padoan, P., Nordlund, A., & Jones, B. J. T. 1997, MNRAS, 288, 145
Pejcha, O., & Thompson, T. A. 2015, ApJ, 801, 90
Rowan-Robinson, M., Oliver, S., Wang, L., et al. 2016, MNRAS, 461, 1100
Shen, H., Toki, H., Oyamatsu, K., & Sumiyoshi, K. 1998, NuPhA, 637, 435
Smartt, S. J. 2009, ARA&A, 47, 63
Smartt, S. J. 2015, PASA, 32, e016
Strigari, L. E., Beacom, J. F., Walker, T. P., & Zhang, P. 2005, JCAP, 4, 017
Strumia, A., & Vissani, F. 2003, PhLB, 564, 42
Sukhbold, T., Ertl, T., Woosley, S. E., Brown, J. M., & Janka, H.-T. 2016, ApJ, 821, 38
Sumiyoshi, K., Yamada, S., & Suzuki, H. 2008, ApJ, 688, 1176
Ugliano, M., Janka, H.-T., Marek, A., & Arcones, A. 2012, ApJ, 757, 69
Vissani, F. 2015, JPhG, 42, 013001
Yüksel, H., & Beacom, J. F. 2007, PhRvD, 76, 083007